A Reconfigurable $Al_2S_3/LuCl_2$ Multiferroic Tunnel Junction with Giant Tunneling Electroresistance and Magnetoresistance for High-Performance Memory

Yunlai Zhu [a], Ke Wang [a], Yong Zhang [a], Chaotong Xie [a], Tao Jiang [a], Zhongren Ye [a], Xiaoling Wu [a], Haotian Tang [a], Xi Sun [a], Tong Zhu [a], Yang Hu [a], Zuyu Xu [a], Zhe Feng [a], Lihua Xu [a], Wendong Lu [a], Zuheng Wu [a], Yuehua Dai [a*]

[a] School of Integrated Circuits, Anhui University, Hefei, Anhui, 230601, China.

Corresponding Authors

*E-mail: daiyuehua@ahu.edu.cn (Y.-H. Dai)

As shown in **Fig. S1**, the optimized monolayer Al_2S_3 crystal structure features a five-atom layered sequence (S–Al–S–Al–S) within the P-3m1 space group. It exhibits two stable ferroelectric polarization states—upward (P↑) and downward (P↓)—corresponding to the configurations in **Figs. S1(a)** and **(b)**, respectively. These polarized states arise from the displacement of the central sulfur atom toward either the top or bottom atomic layer. The plane-averaged electrostatic potential along the out-of-plane direction was calculated for both states (**Figs. S1(c)** and **(d)**), revealing a potential difference (Δ) of 2.22 eV with opposite polarization orientation.

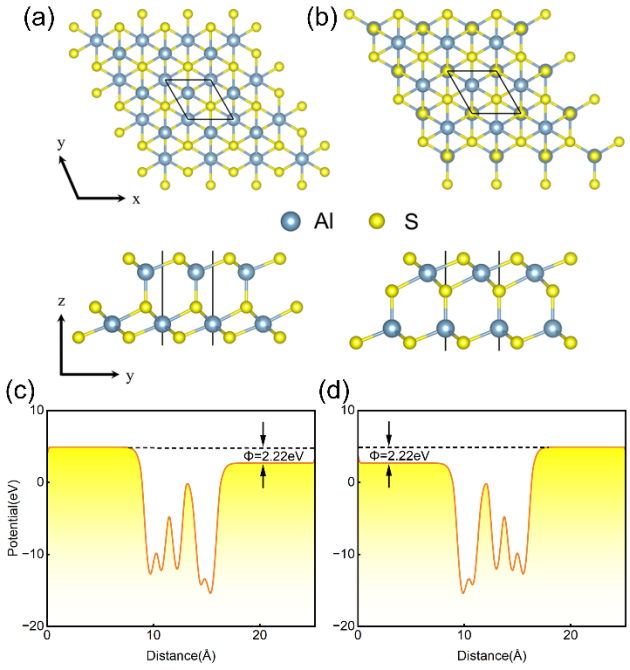

Fig. S1 Top view and side view of (a) Al_2S_3 polarized upward (b) Al_2S_3 polarized

downward. The average potential of Al_2S_3 (c)polarized upward. (d) polarized downward.

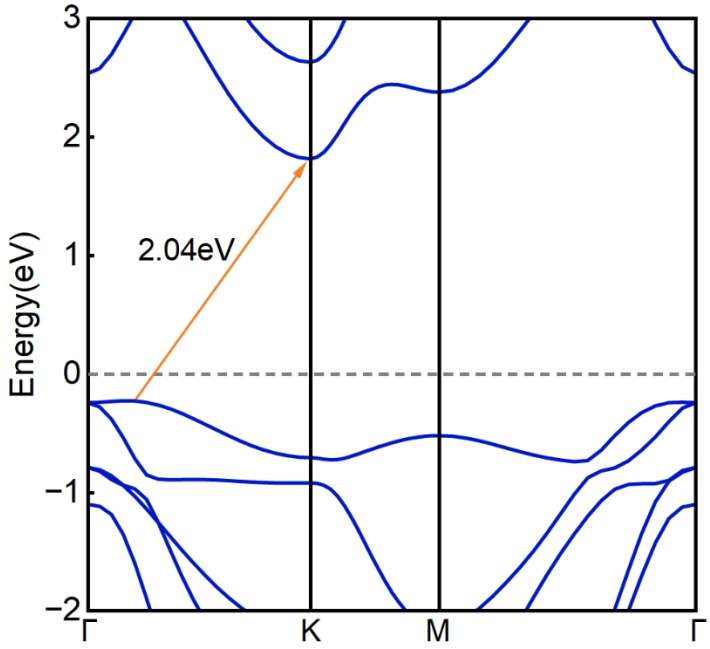

Fig. S2 The band structures of Al_2S_3.

The optimized crystal structure of monolayer $LuCl_2$ is shown in **Fig. S3(a)**, displaying a characteristic sandwich-like unit cell composed of two Cl atomic layers with an intermediate Lu layer. Each Lu atom is octahedrally coordinated by six nearest-neighbor Cl atoms. With an electronic configuration of $5d^16s^2$, each Lu atom carries a theoretical magnetic moment of approximately 1.0 μB, originating from spin-polarized electrons in the 5d and 6s valence orbitals—consistent with typical rare-earth electronic structure. To assess its intrinsic polarization, the plane-averaged electrostatic potential was computed (**Fig. S3(b)**). The identical potential values in the vacuum regions on both sides confirm the absence of an intrinsic polarization field within $LuCl_2$.

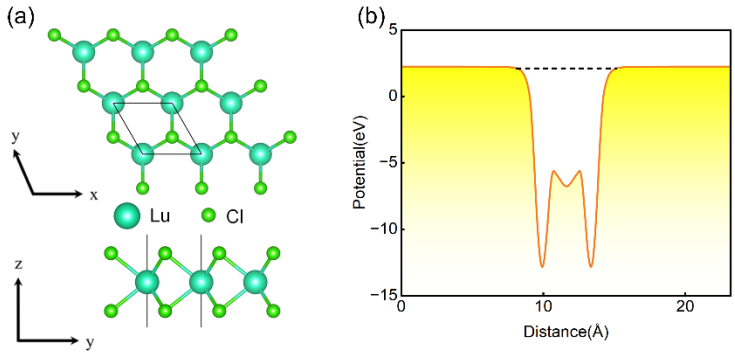

Fig. S3 (a)Top view and side view of $LuCl_2$. (b) The average potential of $LuCl_2$.

The electronic band structure of monolayer $LuCl_2$, calculated using the PBE+U method (U = 3.0 eV applied to Lu *f* orbitals), is shown in **Fig. S4**. $LuCl_2$ exhibits an indirect bandgap of 0.64 eV, with its conduction band minimum (CBM) and valence band maximum (VBM) residing in opposite spin channels.

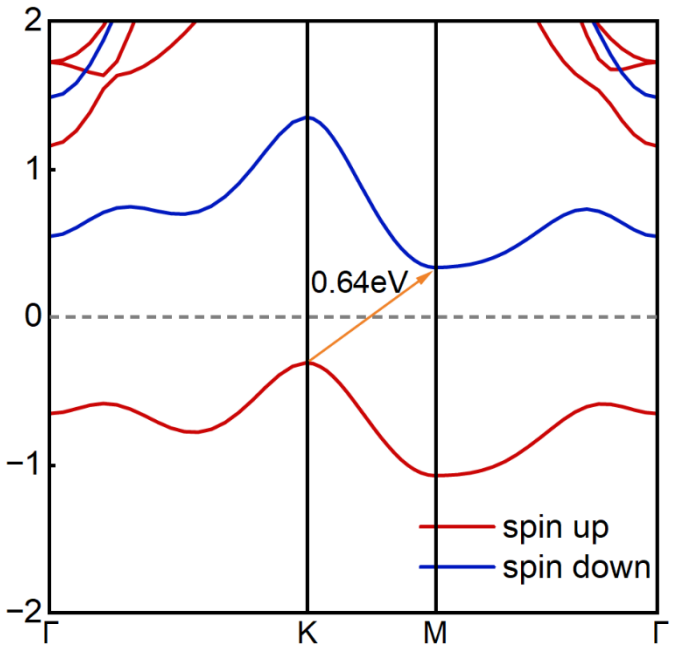

Fig. S4 The band structures of $LuCl_2$: the spin-up and spin-down channels are represented by red lines and blue lines, respectively.

Given the switchable ferroelectric polarization (P↑ and P↓) of the Al_2S_3 monolayer, six distinct stacking models were constructed for the $Al_2S_3/LuCl_2$ heterostructure for each polarization state. An additional six configurations were generated by flipping the $LuCl_2$ monolayer, resulting in a total of twelve stacking models as illustrated in **Fig. S5**.

Table S1 summarizes the computed parameters for these configurations, including total energy (E_{HS}), interfacial layer spacing (d_{HS}), magnetic moment of Lu atoms per unit cell (unit), band gap (E_g), and electrical conductivity. Among all configurations, stacking model VI yields the lowest total energy for both Al_2S_3 polarization states.

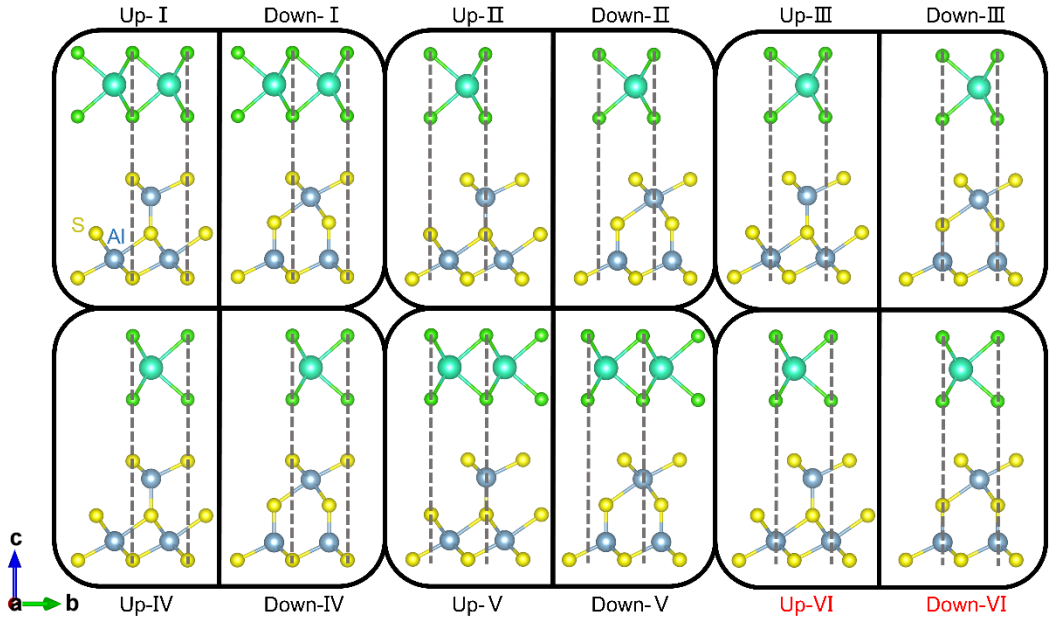

Fig. S5 Six stacking configurations of the heterojunctions formed by Al_2S_3 (with upward/downward polarization) and $LuCl_2$.

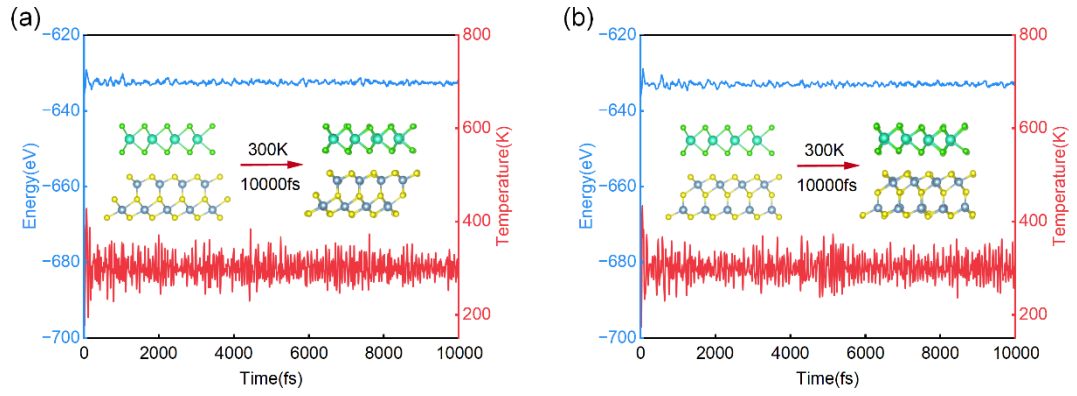

Fig. S6. AIMD simulations of the $Al_2S_3/LuCl_2$ heterostructure at 300 K under (a) P↑ polarization and (b) P↓ polarization. The total energy and temperature are plotted as functions of simulation time. The final structural snapshots at 10 ps confirm structural stability without any phase transition.

Table. S1 Computed parameters of six stacking configurations for $Al_2S_3/LuCl_2$ multiferroic vdW HSs: total energy (E_{HS}, unit: eV); interfacial layer spacing (d_{HS}, unit: Å); magnetic moment of Lu atoms per unit cell (unit: μB); band gap (E_g, unit: eV); and electrical conductivity.

Configurations	**E_{HS}(eV)**	**d_{HS}(Å)**	**M_{Lu}(μB)**	**E_g (eV)**	**Characteristic**
Up-I	-38.870	3.527	0.998	0.569	semiconductor
Down-I	-38.892	3.627	0.970	0	metal
Up-II	-38.903	3.446	0.998	0.577	semiconductor
Down-II	-38.937	3.119	0.964	0	metal
Up-III	-38.905	3.416	0.998	0.555	semiconductor
Down-III	-38.938	3.125	0.964	0	metal
Up-IV	-38.867	3.489	0.999	0.598	semiconductor
Down-IV	-38.891	3.562	0.969	0	metal
Up-V	-38.906	3.368	0.998	0.555	semiconductor
Down-V	-38.935	3.147	0.976	0	metal
Up-VI	-38.909	3.308	0.998	0.574	semiconductor
Down-VI	-38.939	3.115	0.960	0	metal

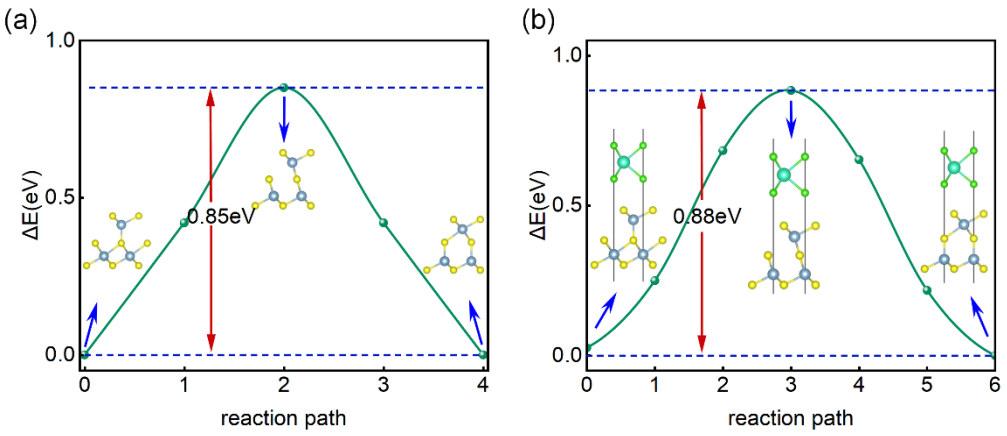

Fig. S7 Total energy distribution along the polarization switching path of (a) the monolayer Al_2S_3 and (b) the $Al_2S_3/LuCl_2$ heterostructure.

DFT calculations were implemented using the VASP package, while NEGF calculations were performed within Quantum ATK. Accordingly, the band structure of the $Al_2S_3/LuCl_2$ heterostructure was calculated using both VASP and ATK. **Figs. S8(a)** and **(b)** show the band structures calculated by VASP, corresponding to the P↑ and P↓ polarization configurations of the ferroelectric layer, respectively. **Figs. S8(c)** and **(d)**

display the band structures obtained by ATK under the same two polarization directions. Comparative analysis reveals that for the P↑ configuration, the band gap calculated by ATK is slightly smaller than that from VASP, while the system still maintains semiconducting characteristics. For the P↓ polarization state, both methods consistently demonstrate the semimetallic nature of the heterostructure. The overall evolution of electronic properties derived from the two methods is highly consistent, fully validating the rationality of the physical mechanism proposed in this work.

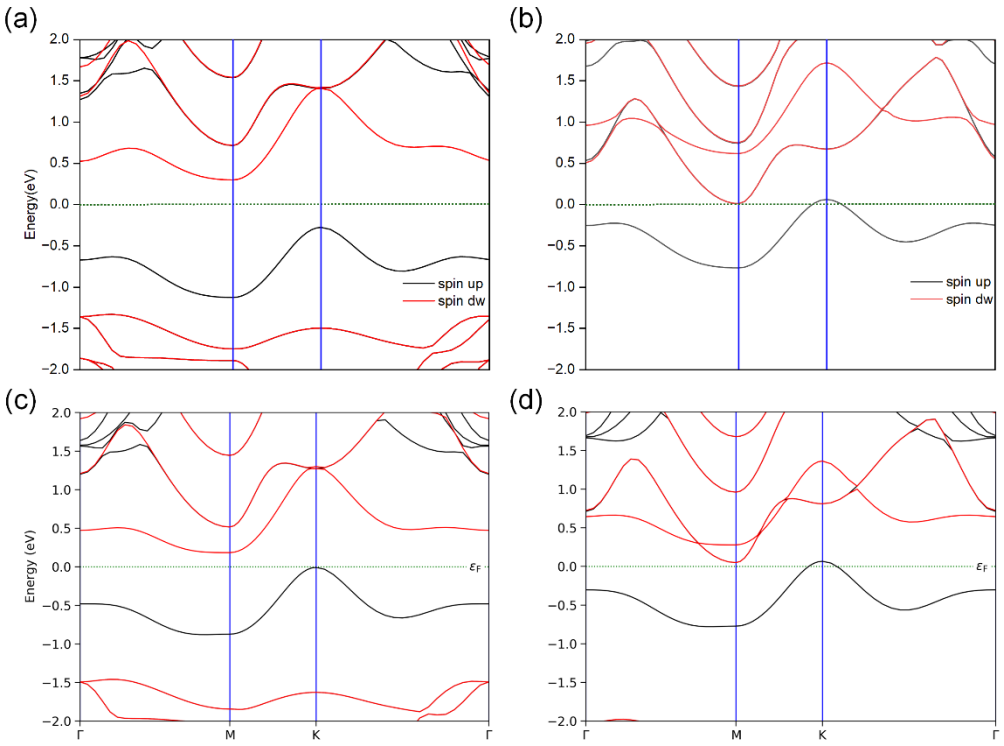

Fig. S8 Band structures calculated by VASP: (a) P↑ polarization, (b) P↓ polarization; band structures calculated by ATK: (c) P↑ polarization, (d) P↓ polarization. The black and red curves denote the spin-up and spin-down channels, respectively. The green dotted line marks the Fermi level, which is set to zero energy.

Based on the linear response method, we constructed a Hubbard U sequence with equal-step linear increment ranging from 0.0 to 6.0 eV. The calculated band structures of the $Al_2S_3/LuCl_2$ heterostructure are displayed in **Fig. S9**. The results indicate that within the entire U value range, under the upward polarization state [**Fig. S9(a)–(g)**], the band gap gradually widens with the increase of the Hubbard U value, and the system always maintains semiconducting characteristics. Under the downward polarization state [**Fig. S9(h)–(n)**], the spin-up channels near the Fermi level gradually shift upward

as the U value rises, while the entire system still exhibits semi-metallic behavior. Notably, the energy bands at the M and K points show a distinct upward shifting trend with increasing U value, which directly manifests the enhanced localization of *f*-electrons. The dependence of the $LuCl_2$ band structure on the Hubbard U value in the heterostructure is highly consistent with that of isolated monolayer $LuCl_2$ reported in previous studies. Together with an analysis of the existing literature and our linear response calculations, we further confirm that U = 3.0 eV is the appropriate choice for this system.[1]

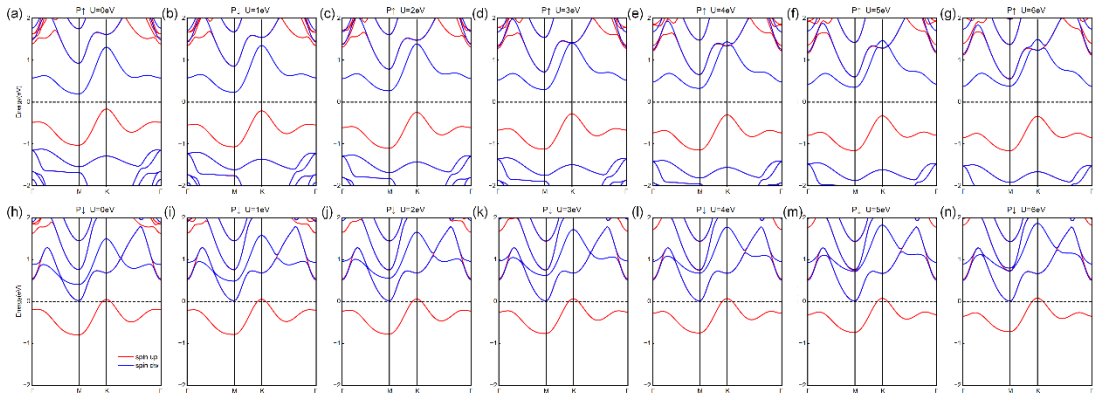

Fig. S9 Electronic band structures of the $Al_2S_3/LuCl_2$ van der Waals heterostructure. (a)-(g) P↑ state with U values ranging from 0 to 6 eV; (h)-(n) P↓ state with U values ranging from 0 to 6 eV.

As shown in **Fig. S10**, by comparing the band structures without and with SOC, we find that the SOC effect barely alters the electronic structure of the $Al_2S_3/LuCl_2$ heterojunction. This further confirms that the reversible semiconductor-to-semimetal transition induced by polarization switching in the $Al_2S_3/LuCl_2$ heterojunction is stable and reliable.

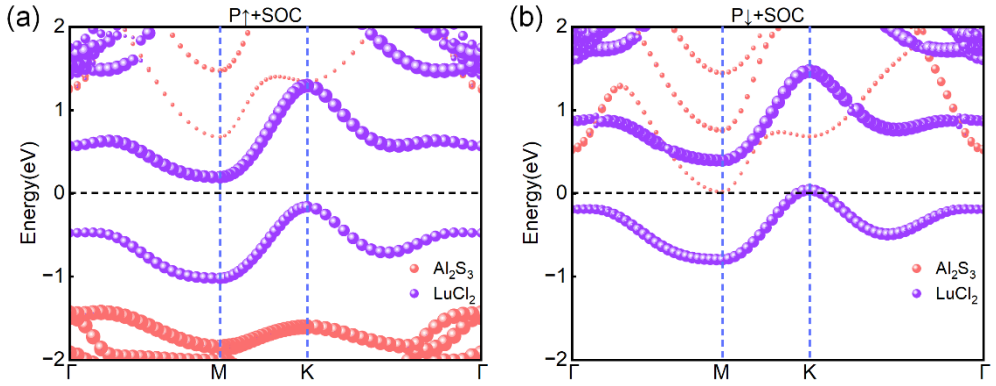

Fig. S10 Band structures of the $Al_2S_3/LuCl_2$ heterostructure with SOC (a) P↑ polarization (b) P↓ polarization.

The HSE06 hybrid functional was employed to compensates for the inherent band-gap underestimation of the PBE scheme. The projected band gaps of Al_2S_3 and $LuCl_2$ are markedly enlarged under both polarization states. Specifically, as illustrated in **Figs. S11** and **S12**, the band gap of Al_2S_3 is 2.05 eV at the PBE level and increases to 2.92 eV at the HSE06 level. For $LuCl_2$, the spin-up and spin-down band gaps are corrected from 1.62 eV and 4.86 eV (PBE) to 2.36 eV and 6.40 eV (HSE06), respectively. Importantly, the fundamental electronic properties predicted by HSE06 are highly consistent with those obtained by PBE. Under P↑ polarization, Al_2S_3 exhibits semiconducting behavior, and both spin channels of $LuCl_2$ remain semiconducting. Under P↓ polarization, Al_2S_3 maintains semimetallic character; while the spin-up channel of $LuCl_2$ is semimetallic and the spin-down channel is semiconducting. This comparison demonstrates that the choice of density functional does not alter the intrinsic electronic properties of the $Al_2S_3/LuCl_2$ heterostructure.

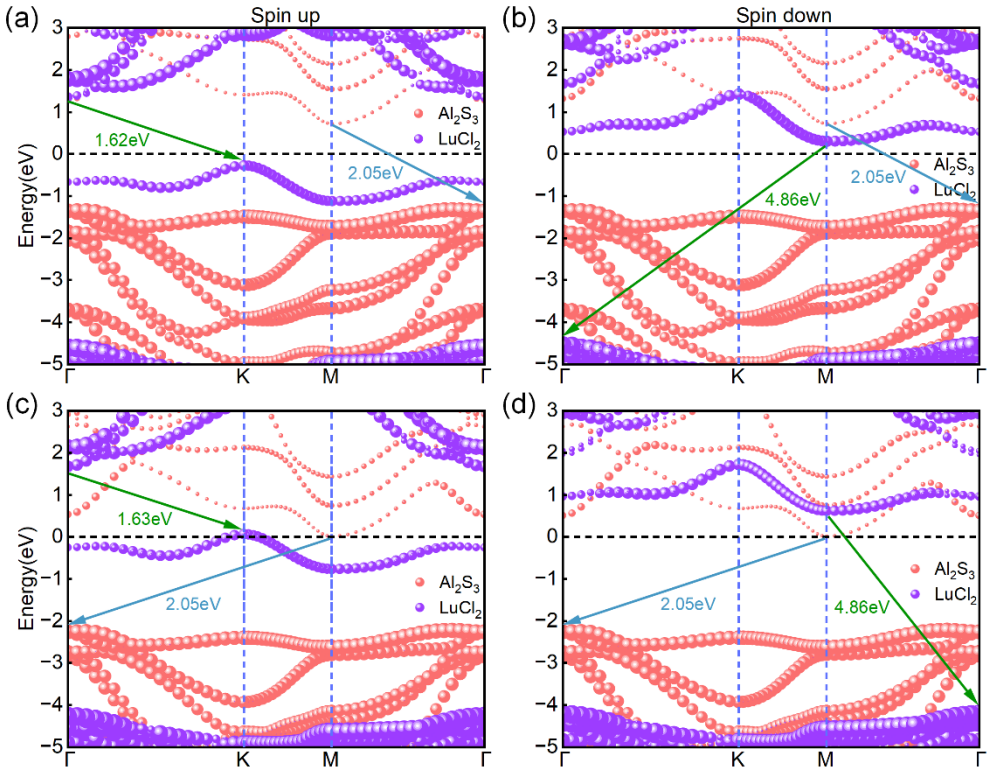

Fig. S11 Electronic band structures of the $Al_2S_3/LuCl_2$ heterostructure with the most stable type-VI stacking configuration, calculated by the PBE functional. (a) Spin-up and (b) spin-down channels under P↑ polarization of Al_2S_3; (c) spin-up and (d) spin-down channels under P↓ polarization of Al_2S_3. The red and purple curves denote the bands derived from the Al_2S_3 and $LuCl_2$ layers, respectively. The green and blue arrows mark the band gaps of $LuCl_2$ and Al_2S_3. The Fermi level is set to zero.

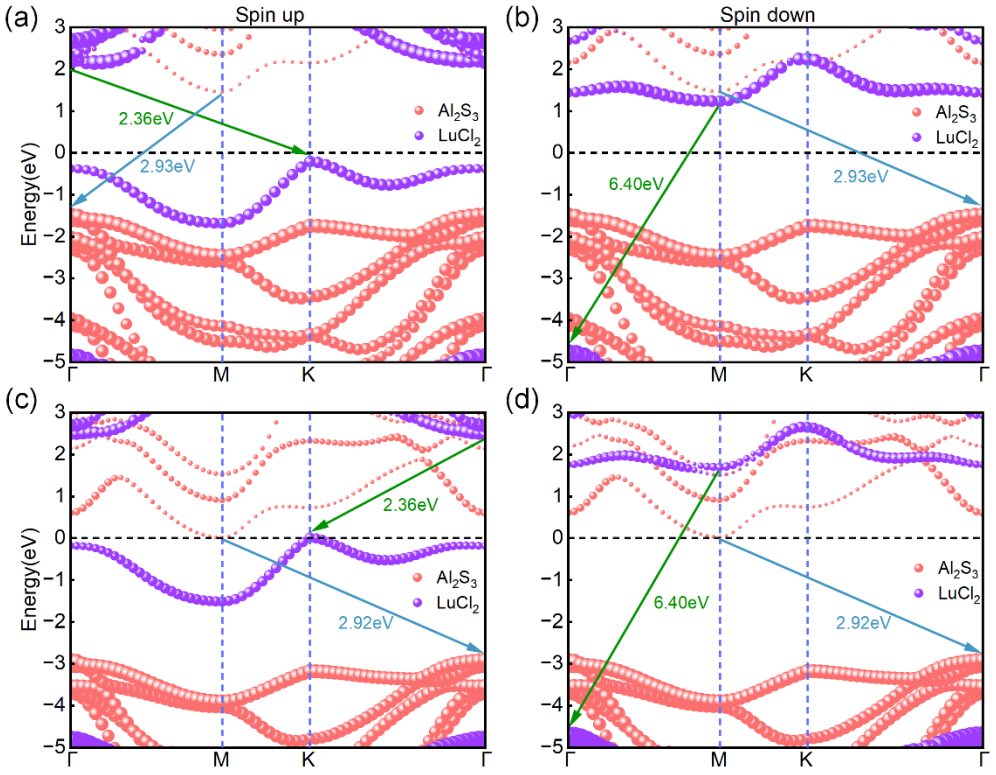

Fig. S12 Electronic band structures of the $Al_2S_3/LuCl_2$ heterostructure with the most stable type-VI stacking configuration, calculated by the HSE06 functional. (a) Spin-up and (b) spin-down channels under P↑ polarization of Al_2S_3; (c) spin-up and (d) spin-down channels under P↓ polarization of Al_2S_3. The red and purple curves denote the bands derived from the Al_2S_3 and $LuCl_2$ layers, respectively. The green and blue arrows mark the band gaps of $LuCl_2$ and Al_2S_3. The Fermi level is set to zero.

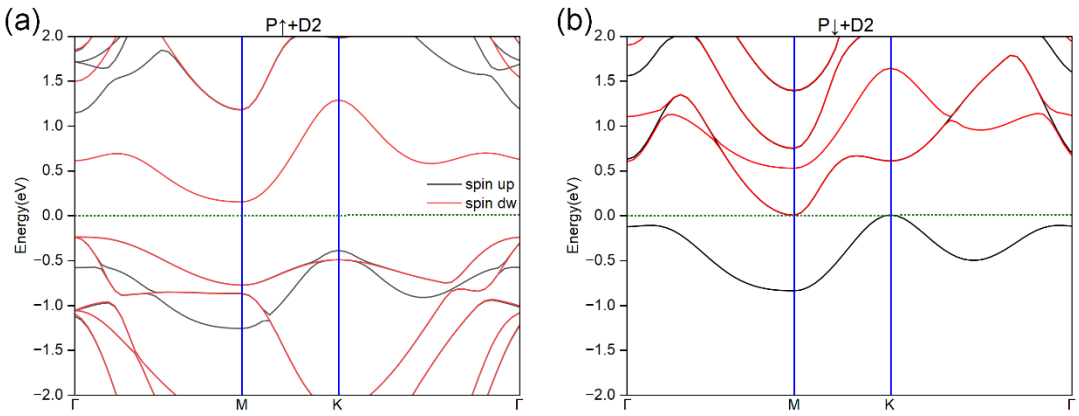

Fig. S13 Band structure of the $Al_2S_3/LuCl_2$ heterostructure with D2 correction: (a) P↑ polarization, (b) P↓ polarization.

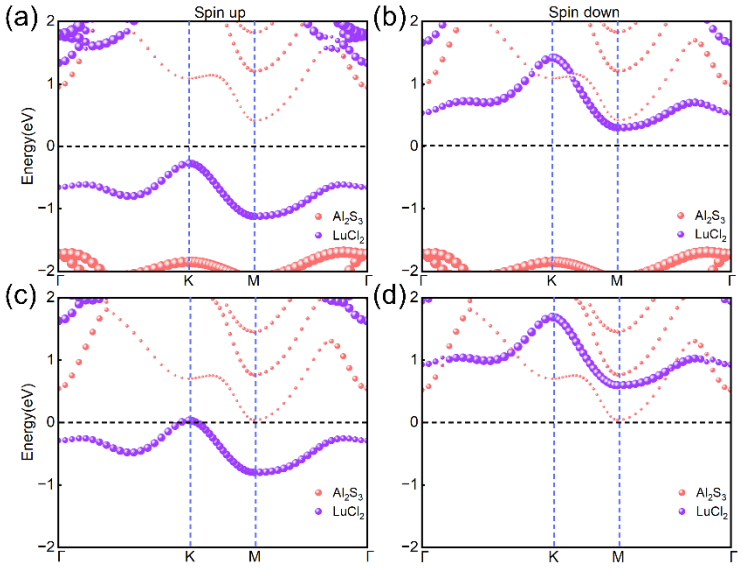

Fig. S14 The $Al_2S_3/LuCl_2$ heterostructure in stacking configuration I with electronic band structures for the (a) spin-up channel and (b) spin-down channels under P↑ polarization, and for the (c) spin-up and (d) spin-down channels under P↓ polarization. Red and purple curves denote bands from the Al_2S_3 and $LuCl_2$ layers, respectively. The Fermi level is set to zero energy.

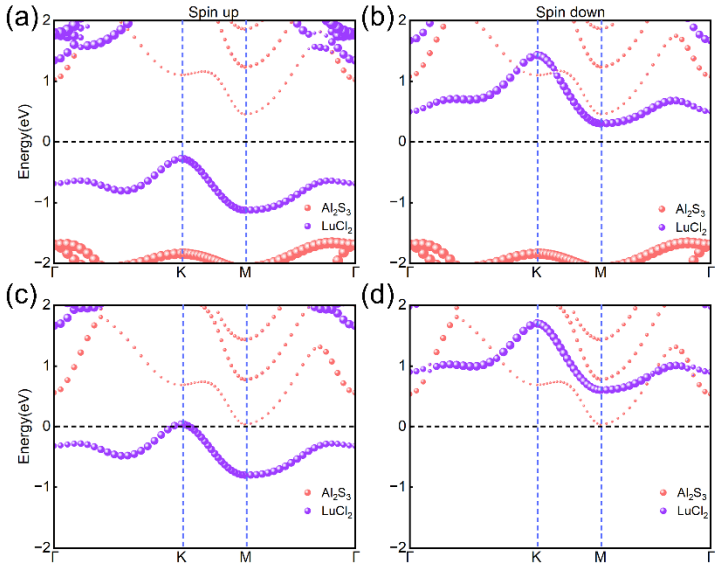

Fig. S15 The $Al_2S_3/LuCl_2$ heterostructure in stacking configuration II with electronic band structures for the (a) spin-up channel and (b) spin-down channels under P↑ polarization, and for the (c) spin-up and (d) spin-down channels under P↓ polarization. Red and purple curves denote bands from the Al_2S_3 and $LuCl_2$ layers, respectively. The Fermi level is set to zero energy.

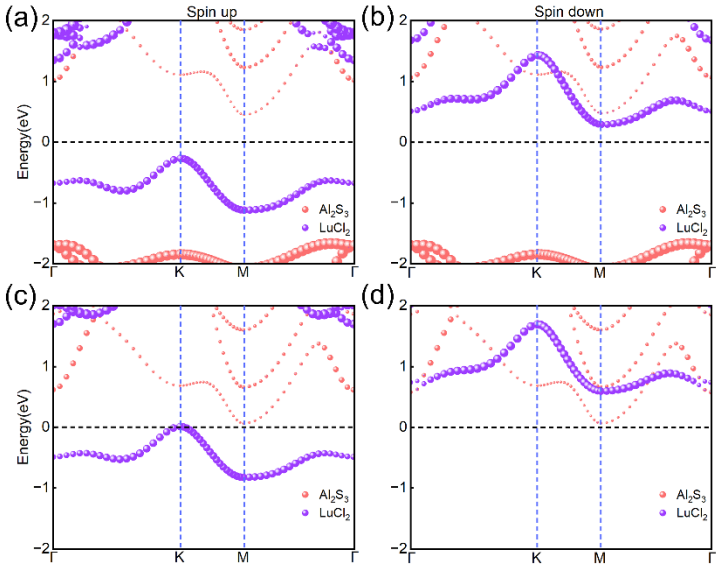

Fig. S16 The $Al_2S_3/LuCl_2$ heterostructure in stacking configuration III with electronic band structures for the (a) spin-up channel and (b) spin-down channels under P↑ polarization, and for the (c) spin-up and (d) spin-down channels under P↓ polarization. Red and purple curves denote bands from the Al_2S_3 and $LuCl_2$ layers, respectively. The Fermi level is set to zero energy.

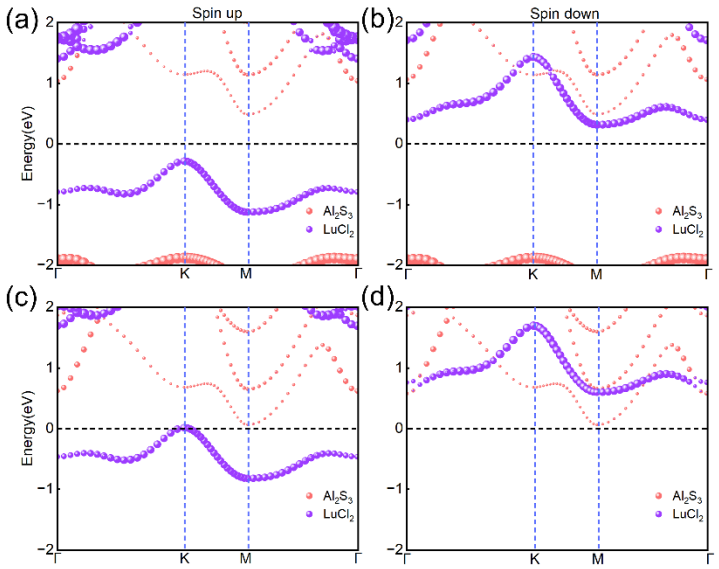

Fig. S17 The $Al_2S_3/LuCl_2$ heterostructure in stacking configuration IV with electronic band structures for the (a) spin-up channel and (b) spin-down channels under P↑ polarization, and for the (c) spin-up and (d) spin-down channels under P↓ polarization. Red and purple curves denote bands from the Al_2S_3 and $LuCl_2$ layers, respectively. The Fermi level is set to zero energy.

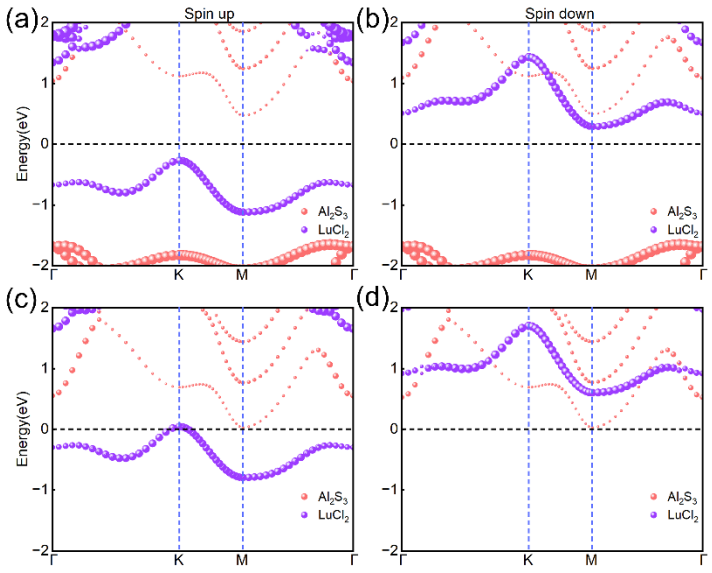

Fig. S18 The $Al_2S_3/LuCl_2$ heterostructure in stacking configuration V with electronic band structures for the (a) spin-up channel and (b) spin-down channels under P↑ polarization, and for the (c) spin-up and (d) spin-down channels under P↓ polarization. Red and purple curves denote bands from the Al_2S_3 and $LuCl_2$ layers, respectively. The Fermi level is set to zero energy.

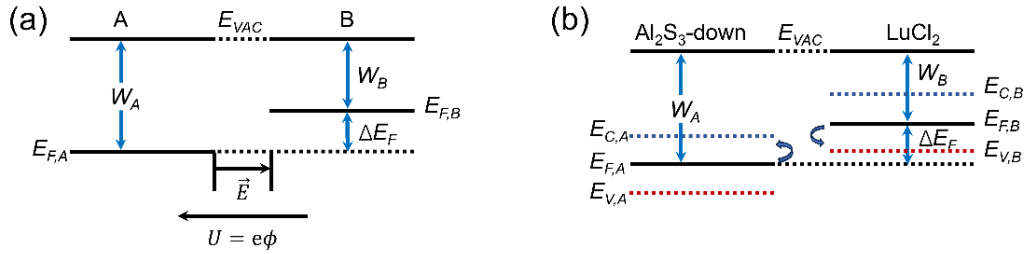

Fig. S19 (a) Schematic model of the formation of contact potential between two different materials. (b) Schematic diagram of the respective band shifts of Al_2S_3 (with downward polarization) and $LuCl_2$ when forming a heterojunction.

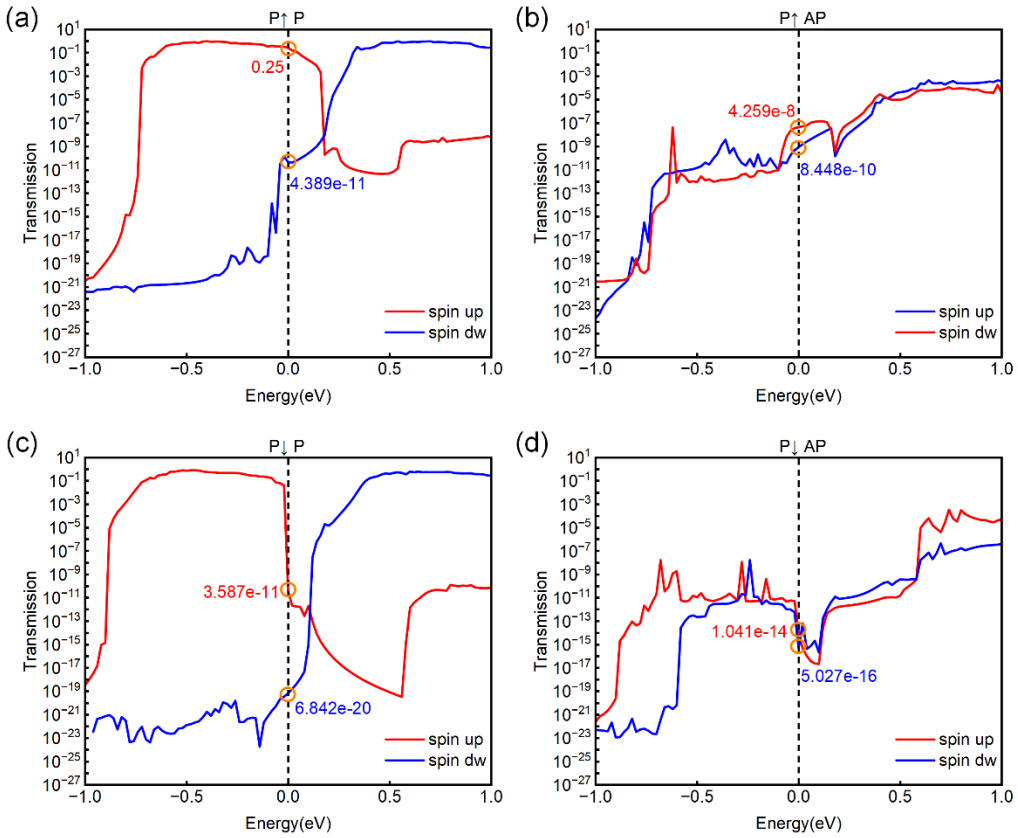

Fig. S20 Electron transmission spectra of the two-probe $Al_2S_3/LuCl_2$ multiferroic tunnel junction with $LuCl_2$ as the central barrier layer: (a) FE P↑/P state, (b) FE P↑/AP, (c) FE P↓/P state, (d) FE P↓/AP state. The red and blue curves represent the spin-up and spin-down channels, respectively.

Table. S2 The evaluated TMR TER and SIE ratios based on different designs of MFTJs.

MFTJ structures	TMR	TER	SIE	Reference
$MnSe_2/Al_2S_3$	83 %	3.18×10^3 %	*	[4]
$VSe_2/Sc_2CO_2/NiClBr/VSe_2$	3.22×10^4 %	1.19×10^3 %	90%	[5]
$In_2Se_3/LaBr_2$	1.62×10^4 %	2.11×10^5 %	99.4%	[6]
$LuCl_2/Al_2S_3$	5.8×10^8 %	7.08×10^{11} %	100%	This work

Table. S3 The evaluated TER ratios based on different designs of FTJs.

FTJ structures	TER	Reference
$SnTe/In_2Se_3$	1.00×10^4 %	[7]
Au/In_2Se_3	10^4 %	[8]
VSi_2N_4/Sc_2CO_2	650%	[9]
$LuCl_2/Al_2S_3$	6.472×10^9 %	This work

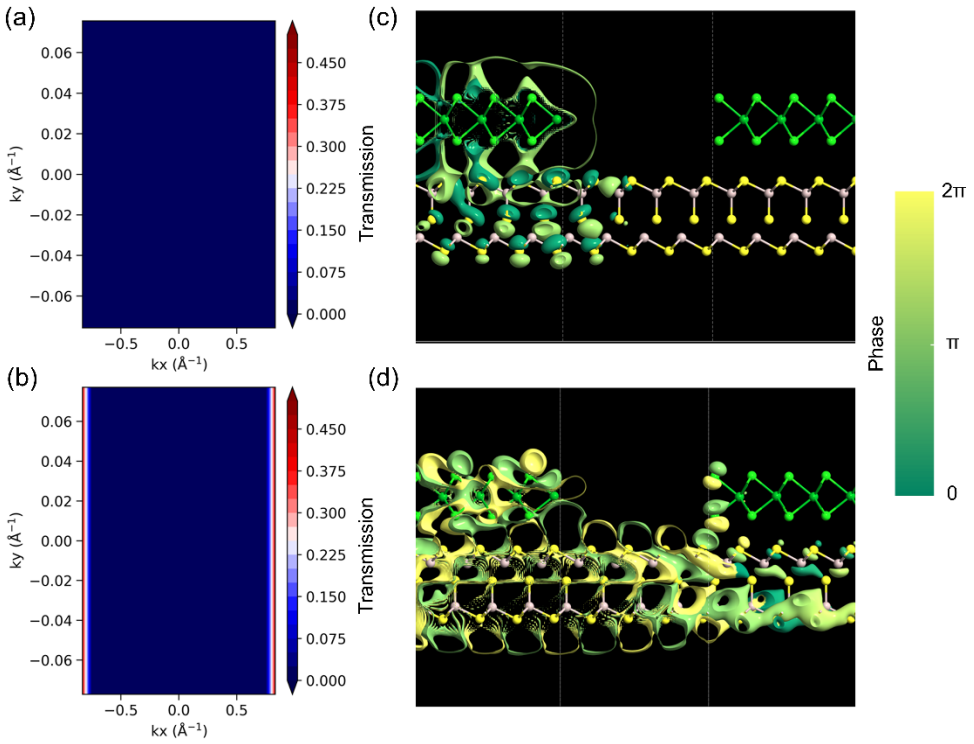

Fig. S21 Transmission spectra of the two-dimensional Brillouin zone for $Al_2S_3/LuCl_2$ MFTJ with N=2 Al_2S_3 as the central barrier at the Fermi level: (a) Al_2S_3 with upward polarization, (b) Al_2S_3 with downward polarization, and the corresponding transmission eigenstates: (c) Al_2S_3 with upward polarization, (d) Al_2S_3 with downward polarization. The isosurface value is 0.03 a.u.

References

1. C.-S. Hu, Y.-J. Wu, Y.-S. Liu, S. Fu, X.-N. Cui, Y.-H. Wang and C.-W. Zhang, *Chin. Phys. B*, 2023, **32**, 037306, DOI:10.1088/1674-1056/ac89d6
2. P. Borlido, T. Aull, A. W. Huran, F. Tran, M. A. L. Marques and S. Botti, *J. Chem. Theory Comput.*, 2019, **15**, 5069-5079, DOI:10.1021/acs.jctc.9b00322
3. K. B. John P. Perdew, * Matthias Ernzerhof, *Phys. Rev. Lett.*, 1996, **77**, 3865-3868, DOI:doi.org/10.1103/PhysRevLett.77.3865
4. L. Li, D. Zou, W. Jia and S. Xie, *Curr. Appl. Phys*, 2025, **80**, 234-241, DOI:10.1016/j.cap.2025.09.022
5. L. Song, D. Chen, Y. Wang, C. Su, Y. Yang and X. Zheng, *Phys. Rev. Appl.*, 2025, **23**, 054085, DOI:10.1103/PhysRevApplied.23.054085
6. X. Zheng, Z. Zheng, S. Yang, C.-S. Liu, L. Zhang and H. Hao, *Phys. Rev. B*, 2024, **110**, 115439, DOI:10.1103/PhysRevB.110.115439
7. Z. Liu, P. Hou, L. Sun, E. Y. Tsymbal, J. Jiang and Q. Yang, *Npj Comput. Mater.*, 2023, **9**, 6, DOI:10.1038/s41524-022-00953-x
8. L. Kang, P. Jiang, H. Hao, Y. Zhou, X. Zheng, L. Zhang and Z. Zeng, *Phys. Rev. B*, 2021, **103**, 125414, DOI:10.1103/PhysRevB.103.125414
9. X. Zhang, B. Liu, J. Huang, X. Cao, Y. Zhang and Z.-X. Guo, *Phys. Rev. B*, 2024, **109**, 205105, DOI:10.1103/PhysRevB.109.205105